

Enhancing Condensation Heat Transfer on Three-Dimensional Hybrid Surfaces

*Ching-Wen Lo, Yu-Cheng Chu, Ming-Han Yan, and Ming-Chang Lu**

Department of Mechanical Engineering, National Chiao Tung University, Hsinchu,
Taiwan 300

*E-mail: mclu@mail.nctu.edu.tw

SUMMARY

In recent years, micro/nanostructured surfaces have been applied to enhance condensation heat transfer. However, condensation heat transfer is greatly deteriorated by the flooding phenomenon that occurs at high subcooling temperatures. Here, we proposed a three-dimensional (3D) hybrid surface to enhance the condensation at high subcooling temperatures. The 3D hybrid surface consisted of superhydrophobic (SHB) Si nanowire (SiNW) arrays and hydrophilic microchannels. The microchannels could confine the liquid film thickness, and the liquid bridges formed on the 3D hybrid surfaces could be self-removed. Both of these characteristics prevent the surfaces from flooding. In addition, liquid droplets formed in the SiNW regions were dragged into the microchannels, which also improved the heat transfer. The heat transfer coefficient on the 3D hybrid surface could be enhanced over a large subcooling range. More remarkably, a record high heat flux of $650 \text{ kW}\cdot\text{m}^{-2}$ was obtained on the 3D hybrid surface.

Keywords: condensation heat transfer, three-dimensional hybrid surface, superhydrophobic Si nanowire array, hydrophilic microchannels, heat transfer coefficient, heat transfer rate, liquid bridge, flooding.

HIGHLIGHTS

1. The liquid films could be confined inside the microchannels.
2. The liquid bridges could be self-removed on the 3D hybrid surface.
3. A record high heat flux of $650 \text{ kW}\cdot\text{m}^{-2}$ was obtained on the 3D hybrid surface.
4. The heat transfer coefficient could be enhanced over a large subcooling range on the 3D hybrid surface.

eTOC BLURB

Given the self-unbridging phenomenon, the confined liquid film thickness, and the dragging mode of droplet departure observed on the 3D hybrid surfaces, enhanced

condensation heat transfer on the 3D hybrid surface over a large subcooling range was achieved. In addition, the obtained heat flux of $650 \text{ kW}\cdot\text{m}^{-2}$ at subcooling temperatures of 18 K exceeded the values in the literature regarding state-of-the-art micro/nanostructured surfaces. This suggests that a 3D hybrid surface can be applied to enhance the condensation in various applications.

CONTEXT & SCALE

Condensation is a liquid-vapor phase change process that is widely seen in various applications such as steam power plants, heat exchanges, energy harvesting, water harvesting, electronics cooling, and dehumidifiers. Enhancing condensation can be achieved by using micro/nanostructured surfaces to promote dropwise condensation. Most of the micro/nanostructured surfaces show enhanced condensation at low surface subcooling temperatures, but the condensation performance deteriorates significantly at high subcooling temperatures. This mainly results from the buildup of a liquid film on the structured surfaces as the subcooling temperature increases.

Nevertheless, many applications require operation at a high degree of subcooling temperature, including distillation plants, industrial refrigeration systems, and steam power plants. Thus, enhancing the condensation at high subcooling temperatures is necessary. Here, by using a three-dimensional (3D) hydrophobic/hydrophilic hybrid surface, for the first time, the condensation heat transfer is enhanced over a wide range of subcooling temperatures from 2–18 K. In addition, a record high heat flux of $650 \text{ kW}\cdot\text{m}^{-2}$ is obtained on the 3D hybrid surface at high subcooling temperatures. The concept of this work can be applied to improve the condensation performance in a wide range of applications involving condensation.

INTRODUCTION

Condensation is a ubiquitous phase-change phenomenon in our daily lives.¹⁻² Condensation is also an essential process in many industrial applications, from large-scale systems such as power plants and water desalination plants to small-scale systems such as micro vapor chambers.³⁻⁶ In addition, condensation plays an important role in water harvesting⁷⁻⁹, solar steam generation¹⁰, and energy harvesting.¹¹ Thus, enhancing condensation efficiency promises considerable savings in energy, capital, and operational costs in many industry fields.¹²⁻¹⁵ It is well-known that surface wettability highly affects condensation. Generally, condensation can be classified into two modes: filmwise condensation (FWC) and dropwise condensation (DWC).

When vapor condenses on a hydrophilic surface, a liquid film forms on the

surface, termed as FWC. As the liquid film covers the condensing surface in the FWC, the thickness of the liquid film can grow by up to 100 μm as the surface subcooling temperature (ΔT_{sub}) increases,¹⁴ which significantly deteriorates the condensation heat transfer owing to the low thermal conductivity (k) of the liquid water ($k \sim 0.6 \text{ W}\cdot\text{m}^{-1}\cdot\text{K}^{-1}$).¹⁶ ΔT_{sub} is the difference between the vapor temperature and the surface temperature. In comparison, DWC can be achieved on a hydrophobic surface. During DWC, gravity-driven condensed droplets can roll off the surface rapidly, refreshing the condensing surface for renucleation, upon which the process can repeat itself and allow for a better condensation heat transfer performance.¹⁷ Compared to FWC, DWC can give a heat transfer coefficient (h) that is one order of magnitude higher.¹⁸

In the last decade, micro/nanostructure-induced superhydrophobic (SHB) surfaces have drawn significant attention for enhancing DWC.¹⁹ An SHB surface typically possesses very low water adhesion with a large water contact angle ($\text{CA} > 150^\circ$) and a small contact angle hysteresis ($\text{CAH} < 10^\circ$). At low ΔT_{sub} , small-sized liquid droplets form on the SHB surface via condensation. The liquid droplets coalesce with each other and induce out-of-plane jumping motions on the surface. This is termed a coalescence-induced jumping motion.²⁰ The jumping motion can efficiently remove small-sized droplets at low ΔT_{sub} .

Meanwhile, on an ordinary hydrophobic surface, the liquid droplets need to grow large enough to be removed by gravity as ΔT_{sub} increases.²¹ Thus, the SHB surface can enhance h at low ΔT_{sub} . To realize the jumping motion on the SHB surface, condensed droplets should stay on top of the micro/nanostructures with air pockets underneath the droplets.²² This is so-called the Cassie state of a liquid droplet. By contrast, if the droplets are in intimate contact with the micro/nanostructures, the droplets are in the Wenzel state. Liquid droplets in the Wenzel state are highly pinned and are difficult to remove from the surface.²³⁻²⁴

As ΔT_{sub} increases, the sizes of the nuclei decrease (on the order of a few nanometers at $\Delta T_{\text{sub}} = 10 \text{ K}$), and the nucleation site density increases.²⁵ The liquid droplets grow between the micro/nanostructures and connect with each other. Thus, the wetting state of the droplets on the SHB surface changes from the suspended Cassie state to the highly pinned Wenzel state as ΔT_{sub} increases. The Wenzel droplets tend to coalesce with each other, and the condensates eventually build up a thick liquid film on the surface as ΔT_{sub} increases. This is considered to be flooding of the surface, which greatly deteriorates the condensation heat transfer on the surface.²⁶⁻²⁸ To avoid the deterioration of the heat and mass transfer efficiency on a surface with increased ΔT_{sub} , one needs to prevent the surface from flooding at high ΔT_{sub} .

Recently, researchers reported that hydrophobic/hydrophilic hybrid surfaces with

a wettability gradient can enhance the condensation efficiency by delaying the flooding.²⁸⁻²⁹ A 2D hybrid surface can alleviate the flooding because the liquid films covering the hydrophilic regions can absorb the condensed droplets from the nearby hydrophobic regions by the wettability gradient to prevent the hydrophobic regions from flooding. However, the liquid bridging phenomenon is observed on 2D hybrid surfaces with an increase in ΔT_{sub} .²⁹ The pinned liquid bridges in the hydrophilic regions cannot be removed by gravity.³⁰ In the end, flooding is observed on conventional 2D hybrid surfaces at high ΔT_{sub} . Hence, enhancing the condensation heat transfer on a hybrid surface at high ΔT_{sub} is still a challenge. Nevertheless, a hybrid surface is a potential candidate for enhancing condensation at high ΔT_{sub} because it can mitigate the flooding.

Thus, a brand-new architecture of the hybrid surface should be proposed to eliminate the liquid bridges at high ΔT_{sub} . Moreover, to enhance the overall condensation efficiency of a hybrid surface, methods for simultaneously promoting DWC and FWC must be considered, especially at high ΔT_{sub} . To achieve efficient DWC, it is essential to have the hybrid surface shed the liquid droplets in the hydrophobic regions efficiently. In addition, the liquid film in the hydrophilic regions should remain thin to reduce its thermal resistance.

Here, we propose a three-dimensional (3D) hybrid surface to enhance the condensation heat transfer over a large range of ΔT_{sub} . Compared to the DWC on an SHB SiNW surface, h on the 3D hybrid surface was enhanced by 130% and 85% at a medium ΔT_{sub} of 8 K and at a high ΔT_{sub} of 18 K, respectively. In addition, the condensation heat flux (q) on the 3D hybrid surface at a high subcooling temperature ($\Delta T_{\text{sub}} \sim 18$ K) was enhanced by 84% from that on the SHB SiNW surface.

The superior heat transfer performance obtained on the 3D hybrid surface at high ΔT_{sub} was attributed to the following reasons: (1) the 3D hybrid surface has a large wettability gradient and a significant structural height difference between the hydrophobic and hydrophilic regions, both of which prevent the condensing surface from flooding at high ΔT_{sub} ; (2) the thickness of the liquid films was confined to ~ 50 μm in the hydrophilic microchannels on the 3D hybrid surface, which reduced the thermal resistance of the liquid films; (3) the departure diameters ($D_d \sim 15$ μm) of condensed droplets in the hydrophobic regions were four times smaller than those on the SHB SiNW surface ($D_d \sim 60$ μm) at high ΔT_{sub} ; and (4) the liquid bridges could be promptly absorbed by the liquid flow in the microchannels on the 3D hybrid surface in a period of ~ 40 ms after their formation, and therefore the flooding at high ΔT_{sub} could be eliminated. A high q of $650 \text{ kW}\cdot\text{m}^{-2}$ and a high h of $37 \text{ kW}\cdot\text{m}^{-2}\cdot\text{K}^{-1}$ at $\Delta T_{\text{sub}} \sim 18$ K were obtained on the 3D hybrid surface. The obtained q exceeds the reported heat flux values for state-of-the-art micro/nanostructured surfaces in the literature.^{1, 27,}

RESULTS AND DISCUSSION

Three-Dimensional Hybrid Surface

Figure 1A shows a schematic of the 3D hybrid surface. The 3D hybrid surface consists of hydrophilic Si microchannels and SHB SiNW arrays. The hydrophilic microchannels have a width S and depth H . **Figure 1B** shows a scanning electron microscope (SEM) image at the sidewall of the microchannel. The hydrophilic Si microchannel has vertical edges, a smooth side wall, and a flat bottom wall. The vertically aligned SiNW arrays were synthesized on top of the walls, which separates the microchannels.

The fabrication procedure for the 3D hybrid surfaces is described in the Experimental Section and in **Figure S1** in the Supplementary Information (SI). A 60-nm-thick Teflon[®] thin layer was coated on the top of the SiNW arrays to render the arrays hydrophobic. **Figure 1C** shows a top-view SEM image of the SiNW array. **Figure 1D** shows a side-view SEM image of the straightly aligned SiNW array, and **Figure 1E** displays an SEM image of a single Si nanowire. The nanowires have a diameter of 50–300 nm and a height of 15 μm . The equilibrium water CA on the hydrophilic Si surface was approximately 30°, whereas the equilibrium water CA on the SiNW arrays was \sim 150°. The contact angle measurements were carried out using the sessile drop method (DSA-100, Oldinburgh Co., Germany).

The equilibrium CA and CAH on the studied surfaces are listed in **Table S1**. A large number of microcavities were identified in the SiNW array. The microcavities were formed during the SiNW synthesis process as a result of the surface tension force, which bundled the nanowires together.³³ The microcavities promote nucleation in condensation. Three 3D hybrid surfaces were investigated. They had the same H of 50 μm and the same hybrid ratio (ϕ) of 1.5 but with different S of 300, 600, and 1300 μm . ϕ is the ratio between the width of the hydrophobic region (*i.e.*, the SiNW array width W) and the width of the hydrophilic region (*i.e.*, the microchannel width S).

The three 3D hybrid surfaces are referred to as S300, S600, and S1300 hereafter. ϕ of 1.5 was employed in this work because the value was suggested as the optimized ratio in the literature.²⁹ The hydrophobic nanowires can provide a large capillary force for promoting the Cassie state of the condensed droplets, which is favorable because the departure size of the condensed droplets can be reduced in the Cassie state.¹⁷

However, the comparatively larger microcavities in the SiNW arrays might be potential places for forming highly pinned Wenzel droplets at high ΔT_{sub} because of the lower energy barrier for nucleation in a larger cavity.³⁴ To prompt Cassie droplets, the microcavity sizes in the SiNW arrays were minimized in a range of 1 to 5 μm in

this work by adopting a method reported in the previous literature for reducing the agglomeration of the SiNW.³³

Departure Dynamics of Condensate

Condensation characteristics on five surfaces were investigated: the 3D hybrid surfaces of S300, S600, and S1300; a hydrophilic plain Si surface (denoted as the plain Si surface hereafter); and an SHB SiNW array surface (denoted as the SiNW surface hereafter). A closed chamber was customized as shown in **Figure S2** for evaluating the condensation characteristics on the surfaces (see Experimental Procedures and **Figure S2** for details).

The condensation processes on the surfaces were investigated by using a high-speed camera (Mega Speed, MS40K). **Figures 2A–2E** show the dynamics and departure modes of the condensate on the surfaces at different subcooling temperatures. **Figure 2A** shows a conventional FWC observed on the hydrophilic plain Si surface. Condensates discretely formed on the surface and flooding was observed at $\Delta T_{\text{sub}} \sim 2$ K. This is owing to the high wettability of the surface. A continuous liquid film fully covered the surface when ΔT_{sub} was increased to 8 K. When ΔT_{sub} was increased to ~ 18 K, a thicker liquid film formed on the surface. The liquid film was drained away from the surface by gravity at the bottom of the surface (see **Movie S1**).

DWC was observed on the superhydrophobic SiNW surface, as shown in **Figure 2B**. Condensed droplets were randomly distributed on the surface at a low $\Delta T_{\text{sub}} \sim 2$ K. It was found that the major departure mode of the condensed droplets at a low ΔT_{sub} was an out-of-plane jumping motion with a departure diameter D_d smaller than 0.5 mm. The out-of-plane jumping motion is attributed to the release of surface free energy when the droplets that coalesced with each other on the SiNW surface.³⁵ The diameter of the liquid droplets increased as ΔT_{sub} increased to ~ 8 K (**Figure 2B**).

The main condensate departure mode changed from a jumping motion to a gravity-driven sliding motion at $\Delta T_{\text{sub}} \sim 8$ K. Large droplets were observed on the surface, and droplets of tens of millimeters in size slid along the surface. As ΔT_{sub} further increased to ~ 18 K, droplets of size >50 mm were observed, and they coalesced with each other to form a thick film on the surface. Eventually, flooding was observed on the SiNW surface (see **Movie S2**). The flooded SHB surface caused an irreversible condensation transition from the DWC mode to the FWC mode because the formed thick film could not be completely emptied from the condensing surface by gravity at a high ΔT_{sub} .

Figure 2C shows the schematics of the departure dynamics on 3D hybrid surfaces at low and medium-to-high ΔT_{sub} , respectively. At $\Delta T_{\text{sub}} \sim 2$ K, liquid droplets

were indiscriminately condensed in the microchannels and in the SiNW arrays. Jumping and sliding motions occurred concurrently on the 3D hybrid surfaces. The gravity-driven droplets slid along the microchannels, whereas a coalescence-induced jumping motion was observed in the SHB SiNW arrays on the 3D hybrid surfaces. On the 3D hybrid surfaces, when ΔT_{sub} increased to ~ 8 or ~ 18 K, FWC occurred in the hydrophilic regions (*i.e.*, the microchannels), whereas DWC took place in the superhydrophobic SiNW array regions. A continuous liquid film formed in the microchannels, and the liquid drained to the ends of the microchannels by gravity. Meanwhile, the jumping motion in the SiNW arrays changed to a dragging motion at medium to high ΔT_{sub} . Larger droplets in the SiNW arrays were dragged into the microchannels and slid along the microchannels.

Figures 2D–2F show condensation images taken on the S300, S600, and S1300 surfaces at different ΔT_{sub} , respectively. It is worth mentioning that there was no flooding phenomenon observed on the 3D hybrid surfaces at low to high ΔT_{sub} (see **Movies S3, S4, and S5** for the S300, S600, and S1300 surfaces, respectively). Nevertheless, liquid bridges were identified on the S300 and S600 surfaces, as shown in **Figures 2D–2E**.

Figure 2F shows the number of liquid bridges on the S300 and S600 surfaces at the three different values of ΔT_{sub} . Given the small W on the S300 surface, a large number of liquid bridges formed between the microchannels on the surface, and the liquid bridges covered the SiNW arrays at low to medium ΔT_{sub} (see **Figure 2D**). In comparison, given the larger W on the S600 surface, a smaller number of liquid bridges was observed on the S600 surface (see **Figure 2E**). Moreover, almost no liquid bridges were observed on the S1300 surface from $\Delta T_{\text{sub}} \sim 2$ – 18 K provided that S1300 possessed the largest W among the hybrid surfaces (see **Figure 2F**).

Figures 2H and 2I show condensation images taken of the SiNW arrays on the S300 surface at a low ΔT_{sub} of 2 K and at a high ΔT_{sub} of 18 K, respectively. Jumping motions of the liquid droplets were observed in the SiNW array at low ΔT_{sub} (see **Figure 2H**), whereas the sliding motion of liquid droplets was observed at high ΔT_{sub} (see **Figure 2I**).

From the two images shown in **Figure 2H**, one can conjecture that the vanished droplet (the red cycle one) was not removed by sliding or dragging motions because the other droplets surrounding the vanished droplets were not altered. This indicates the jumping motion of the vanished droplet in the SiNW array. The lowercase letters (*i.e.*, a, b, c, d, e, and f) in **Figure 2I** indicate the condensed droplets in the SiNW arrays on the S600 surface. The hydrophilic microchannels were between the SiNW arrays. The white lines represent the meniscus of the liquid films at the edges of the microchannels.

The blurring and disturbance of the white lines in the middle image of **Figure 2H** suggest that the liquid droplets in the SiNW arrays were absorbed into the liquid films through the meniscus. Eventually, the liquid droplets were completely absorbed by the liquid films in the microchannels, as shown in the right-hand image of **Figure 2I**. The a, b, and c droplets were absorbed into the hydrophilic microchannel in the first 20 ms after nucleation; and the d, e, and f droplets were dragged into the microchannel in 40 ms after nucleation. The dragging of the liquid droplets into the microchannels left a fresh surface for renucleation in the SiNW arrays on the 3D hybrid surface.

Confined Liquid Film and Self-Unbridging

Figure 3A shows schematic diagrams of the condensate on a 2D hybrid surface at different ΔT_{sub} . As shown in **Figure 3A-1**, liquid films formed in the hydrophilic regions, and liquid droplets formed in the hydrophobic regions at low ΔT_{sub} . However, at high ΔT_{sub} , liquid bridges forming between the hydrophilic regions and covering the hydrophobic regions were observed (see **Figure 3A-2**). The formation of liquid bridges on top of the hydrophobic regions disables the function of the hydrophobic regions and worsens the heat transfer at high ΔT_{sub} . The liquid bridges eventually led to irreversible flooding condensation (see **Figure 3A-3**), which deteriorated the heat transfer performance at high ΔT_{sub} .²⁹

Figure 3B shows schematic diagrams of the condensate on the 3D hybrid surface and the corresponding condensation images taken on the 3D hybrid surface at different ΔT_{sub} . The main idea of the design of the 3D hybrid surface was to create an additional height dimension on the traditional 2D hybrid surface. The corresponding condensation images taken on the S300 surface at $\Delta T_{\text{sub}} \sim 8$ K proved that the meniscus of the liquid film was pinned at the top edge of the channel owing to the large wettability gradient and the height difference between the hydrophobic and hydrophilic regions. The film thickness was limited to ~ 50 μm in the microchannel on the S300 surface during the condensation, which can prevent the surface from flooding (see **Figure 3B-1**).

When ΔT_{sub} increased to ~ 18 K, a liquid bridge formed on the 3D hybrid surfaces (see **Figure 3B-2**). The corresponding condensation images were taken on the S600 surface at the ΔT_{sub} . A liquid bridge linking the two hydrophilic microchannels (outlined by a blue solid line) was observed on the S600 surface (see **Figure 3B-2**). The size of the liquid bridge became smaller after 20 ms of formation (see **Figure 3B-3**). The liquid bridge completely disappeared after 40 ms of formation (see **Figure 3B-4**). The self-removal of the liquid bridge was termed as self-unbridging. This phenomenon has never been reported.

Figure 3C shows side- and top-view schematic diagrams of the liquid bridge on the 3D hybrid surface. Based on the Bernoulli equation, the high film velocity (v) in the microchannels creates a large pressure difference between the center and edge of the liquid bridge ($\Delta P = P_2 - P_1$), resulting in water flow from the center of the liquid bridge to the liquid film in the microchannel. Thus, the liquid bridge can be absorbed into the microchannels on the 3D hybrid surface.

Figure 3D shows the measured downflowing liquid film velocities on the 3D hybrid surfaces at $\Delta T_{\text{sub}} \sim 18$ K. The dashed line in **Figure 3D** represents the theoretical v on a plain surface in the FWC. By balancing the gravity force and the viscous force at the prescribed conditions, the theoretical v of $6 \text{ cm}\cdot\text{s}^{-1}$ can be obtained. The experimental method for determining v and the theoretical prediction of v are described in the Experimental Procedures.

Figure 3D shows that the film velocities in the microchannels on the 3D hybrid surfaces were more than five times faster than that on a conventional 2D hybrid surface in the FWC mode. The high liquid v presumably occurred because a large number of liquid droplets were dragged into the microchannels, and the liquid film thickness was constrained by the microchannels. Thus, the liquid bridges could be promptly absorbed into the microchannels. Eventually, the liquid bridges were eliminated without needing an external force. The self-unbridging phenomenon observed on the 3D hybrid surfaces can also prevent the surfaces from flooding at high ΔT_{sub} .

Quantitative Analysis

The condensation heat transfer performance depends not only on the departure droplet diameter but also the flooding area. Thus, we quantitatively analyzed D_d and the flooding area ratio (ε) at ΔT_{sub} of 2, 8, and 18 K. **Figures 4A** and **4B** present D_d and ε on the surfaces at the three values of ΔT_{sub} , respectively. D_d in **Figure 4A** was evaluated from the droplets removed by the sliding, dragging, and jumping motions. At a low $\Delta T_{\text{sub}} \sim 2$ K, the dark- and light-colored bars indicate D_d for the jumping mode and D_d for the sliding mode, respectively.

At medium and high ΔT_{sub} , the dark and light colored bars represent D_d for the dragging mode and D_d for the sliding mode, respectively. D_d on the plane Si surface could not be obtained because the surface remained to be flooded at the three values of ΔT_{sub} (see **Figure 2A**). The dashed gray line in **Figure 4A** indicates the capillary length (L_c). $L_c \sim (\sigma/\rho g)^{0.5}$ is the scaling length that balances gravity and the surface tension force. L_c is the theoretical droplet departure diameter of the sliding mode on a vertically orientated hydrophobic surface, and serves as a threshold value to identify flooding.

At low $\Delta T_{\text{sub}} \sim 2$ K, on the SHB SiNW surface, $D_d \sim 0.5$ mm was obtained for the jumping mode, and $D_d \sim 1.9$ mm was obtained for the sliding mode. For the 3D hybrid surfaces, DWC and FWC occurred concurrently on these surfaces. $D_d \sim 0.5$ mm of the jumping mode was obtained in the SHB SiNW array regions. In addition, $D_d \sim 2.4$, 1.7, and 1.3 mm of the sliding mode were obtained in the hydrophilic microchannels on the S300, S600, and S1300 surfaces, respectively.

At $\Delta T_{\text{sub}} \sim 8$ K, on the SHB SiNW surface, the liquid droplets completely transferred their jumping motions into sliding motions. On the 3D hybrid surfaces, in the SiNW regions, the liquid droplets transferred their jumping motions into dragging motions (dark color bars now represent D_d of the dragging mode). Meanwhile, in the microchannels on the 3D hybrid surfaces, the liquid droplets continuously slid along the microchannels (light-colored bars represent D_d of the sliding mode).

The obtained $D_d \sim 4.75$ mm on the SiNW surface was much larger than that ($D_d < 2$ mm) on the 3D hybrid surfaces. Moreover, D_d on the SiNW surface was beyond the flooding threshold (*i.e.*, L_c), indicating that the condensation mode on the SiNW surface transferred to the flooding DWC. The larger D_d on the SiNW surface was a result of the wetting transition from the Cassie state to the Wenzel state or to a partial Wenzel state because of the increase in ΔT_{sub} . Contrastingly, D_d on the 3D hybrid surfaces remained smaller than the flooding threshold at a medium ΔT_{sub} . The droplets in the SiNW array regions on the 3D hybrid surface could be dragged into the microchannels.

Although D_d of the dragging mode (dark color bars) increased with increasing W , a large W on the S1300 surface could decrease the number of liquid bridges and reduce D_d of the sliding mode on the S1300 surface. Thus, the maximum D_d on the S1300 surface was the smallest among those of the 3D hybrid surfaces at $\Delta T_{\text{sub}} \sim 8$ K. It was found that D_d of the dragging mode and D_d of the sliding mode were almost the same on the S1300 surface at $\Delta T_{\text{sub}} \sim 8$ K.

As ΔT_{sub} further increased to 18 K, owing to the increase in the flooding area, the droplet sliding motion on the SiNW surface almost disappeared, and large liquid droplets were found on the SiNW surface (see **Figure 2B**). The obtained $D_d \sim 60$ mm on the SiNW surface was 400% larger than that on the 3D hybrid surfaces ($D_d \sim 1.5$ mm). By contrast, on the 3D hybrid surfaces, D_d of the dragging mode remained small.

In addition, D_d of the sliding mode on the S300 and S600 surfaces decreased with ΔT_{sub} . This was mainly owing to the more pronounced self-unbridging effect as ΔT_{sub} increased, which reduced D_d of the sliding mode on the S300 and S600 surfaces. In addition, there was no error bar for D_d of the sliding mode on the S1300 surface. This was a result of the confined droplet sliding size in the microchannels on

the S1300 surface from low to high ΔT_{sub} .

Figure 4B shows the obtained ε on the SHB SiNW and 3D hybrid surfaces. ε is an area ratio of the flooding area to the overall projection area of the surfaces. The flooding area was defined as the total projected area including the liquid droplets, liquid bridges, and liquid films when their characteristic lengths were larger than the flooding threshold ($L_c \sim 2.66$ mm). In addition, the areas of accumulated liquid at the bottoms of the condensation surfaces on the 3D hybrid surfaces were included in the flooding area. Note that the average ε on the plain Si surface was $\sim 100\%$ over a range of ΔT_{sub} from 2–18 K. Thus, it was not plotted in **Figure 4B**.

At low $\Delta T_{\text{sub}} \sim 2$ K, the lowest $\varepsilon \sim 5\%$ on the SiNW surface was obtained owing to the efficient jumping and sliding motions of the liquid droplets on the SHB SiNW. By contrast, ε on the 3D hybrid surfaces was much higher because approximately 40% of the hydrophobic region was replaced by hydrophilic microchannels to achieve DWC and FWC concurrently on the 3D hybrid surfaces.

At a low $\Delta T_{\text{sub}} \sim 2$ K, ε values of 18% and 15% were found on the S600 and S1300 surfaces because the liquid film was not established in the microchannels on the two surfaces (see **Figures 2E** and **2F**). Meanwhile, on the S300 surface, the obtained ε was around 55% over a ΔT_{sub} range of 2 K to 18 K. The ε of 55% was higher than the prescribed 40% on the S300 hybrid surfaces. This resulted from the formation of liquid bridges on the S300 surface (see **Figures 2D** and **2G**).

When ΔT_{sub} was raised to 8 K, a significant increase in ε (up to $\sim 70\%$) was observed on the SiNW surface owing to the increased number of pinned Wenzel droplets accompanied with a large D_d on the SiNW surface (see **Figures 2B** and **4A**). ε on the S600 and S1300 surfaces increased to 37% and 18%, respectively, owing to the increased liquid film area in the microchannels as ΔT_{sub} increased (see **Figures 2E** and **2F**).

As ΔT_{sub} increased to 18 K, a high $\varepsilon \sim 90\%$ was found on the SHB SiNW surface; therefore, flooding was identified on the SiNW surface (see **Figure 2B**). For the 3D hybrid surfaces, compared to the ε of 55% on the S300 surface, small ε values of $\sim 54\%$ and $\sim 46\%$ were obtained on the S600 and S1300 surfaces, respectively. Although ε also increased with ΔT_{sub} on the S600 and S1300 surfaces, a wider W on the two surfaces can prevent the surfaces from growing liquid bridges at a high ΔT_{sub} , thus alleviating bridging-induced flooding on the surfaces.

Moreover, D_d and ε on the 3D hybrid surfaces can be tailored by W . For example, the maximum D_d on the S300, S600, and S1300 surfaces at $\Delta T_{\text{sub}} \sim 2$ K were 2.0, 1.6, and 1.3 mm, respectively, whereas ε on the S300, S600, and S1300 surfaces was 55%, 37%, and 18%, respectively, at ΔT_{sub} of 8 K. By increasing W on the 3D hybrid surfaces, the maximum D_d and ε can be reduced. A small D_d and ε , as well as a

confined liquid film thickness, can promote h on the 3D hybrid surfaces.

Condensation heat transfer on 3D hybrid surfaces

Figures 4C and 4D show h and the q as a function of ΔT_{sub} on the studied surfaces. The values of h and q in the figures are the averaged values obtained from three repeated experiments, and the error bars correspond to the standard derivations. The data reduction, uncertainty analysis, and heat loss analysis can be found in the SI. The hydrophilic plain Si surface served as a reference surface for comparison.

In **Figures 4C and 4D**, the gray solid circles are h and q obtained on the plain Si surface, and the black solid line is the theoretical prediction from the Nusselt theory. The experimental result on the plain Si surface and the theoretical prediction from the Nusselt theory agreed well with each other, which validated the accuracy of our experiments. The triangle, square, pentagonal, and hexagonal solid symbols in **Figures 4C and 4D** represent h and q obtained on the SiNW, S300, S600, and S1300 surfaces, respectively.

First, the descending trend of h with ΔT_{sub} on all of the studied surfaces was mainly owing to the increase in ε with ΔT_{sub} because liquid water possesses a poor thermal conductivity of $\sim 0.6 \text{ W}\cdot\text{m}^{-1}\cdot\text{K}^{-1}$ (see **Figure 4B**).¹⁴

At low $\Delta T_{\text{sub}} \sim 2 \text{ K}$, DWC was observed on the SiNW surface and in the SiNW array regions on the 3D hybrid surfaces. As a result of the jumping motion associated with a small $D_d < 0.5 \text{ mm}$, a low ε of $\sim 5\%$ was obtained on the SiNW surface among all of the studied surfaces. Hence, the highest h of $\sim 68 \text{ kW}\cdot\text{m}^{-2}\cdot\text{K}^{-1}$ was obtained on the SiNW surface at a low ΔT_{sub} . Meanwhile, given that parts of the hydrophobic regions were replaced by hydrophilic microchannels on the 3D hybrid surfaces, ε of S600 and S1300 was slightly higher than that on the SiNW surface. Thus, the obtained h values on the 3D hybrid surfaces were lower than that on the SiNW surface at a low ΔT_{sub} .

Moreover, as a result of a large number of liquid bridges formed on the S300 surface, the S300 surface had the highest ε at a low ΔT_{sub} (see **Figure 2D**). The larger W on the S1300 and S600 surfaces resulted in a small number of liquid bridges. Thus, a smaller ε was found on the S1300 and S600 surfaces than that on the S300 surface (see **Figures 2E and 2F**). Consequently, higher h values of $49 \text{ kW}\cdot\text{m}^{-2}\cdot\text{K}^{-1}$ and $41 \text{ kW}\cdot\text{m}^{-2}\cdot\text{K}^{-1}$ were obtained on the S1300 and S600 surfaces, respectively, as compared to the h of $23 \text{ kW}\cdot\text{m}^{-2}\cdot\text{K}^{-1}$ on the S300 surface.

When ΔT_{sub} increased to 8 K , given that D_d on the SiNW surface increased (*i.e.*, $D_d \sim 4.8 \text{ mm}$) more than the flooding threshold (*i.e.*, L_c), a noticeable increase in ε was observed, and therefore a significant decrease in h ($\sim 22 \text{ kW}\cdot\text{m}^{-2}\cdot\text{K}^{-1}$) was obtained on the SiNW surface. Meanwhile, given the confined liquid film in the microchannels

and the effective dragging motion of liquid droplets on the SiNW arrays, ε and the maximum D_d on the 3D hybrid surfaces were lower than those on the SiNW surface (**Figures 4A and 4B**). Therefore, the obtained h of 27, 40, and 53 $\text{kW}\cdot\text{m}^{-2}\cdot\text{K}^{-1}$ on the S300, S600, and S1300 surfaces were 22, 81, and 140% higher than h on the SiNW surface, respectively, at $\Delta T_{\text{sub}} \sim 8$ K.

Further increasing ΔT_{sub} to 18 K results in a very large D_d (~ 60 mm) obtained on the SiNW surface. ε on the SiNW surface increased to $\sim 90\%$ and flooding was identified on the surface. This resulted in a low $h \sim 19$ $\text{kW}\cdot\text{m}^{-2}\cdot\text{K}^{-1}$ on the SiNW surface. However, h was still higher than the h (13 $\text{kW}\cdot\text{m}^{-2}\cdot\text{K}^{-1}$) on the plain Si surface because ε on the SiNW surface was lower than the ε of 100% on the plain Si surface.

Meanwhile, given the successful confinement of the flooding area and the reduction of D_d on the 3D hybrid surfaces, ε was maintained at lower than 60% at $\Delta T_{\text{sub}} \sim 18$ K. Thus, the obtained h values of 27 and 29 $\text{kW}\cdot\text{m}^{-2}\cdot\text{K}^{-1}$ on S300 and S600 were 35 and 45% higher than h (~ 20 $\text{kW}\cdot\text{m}^{-2}\cdot\text{K}^{-1}$) on the SiNW surface, respectively. Remarkably, a significant improvement in h was observed on the S1300 surface at $\Delta T_{\text{sub}} \sim 18$ K because the S1300 surface possessed the smallest maximum D_d and ε among all of the studied surfaces at a high subcooling temperature. h of 37 $\text{kW}\cdot\text{m}^{-2}\cdot\text{K}^{-1}$ obtained on the S1300 surface was 213% and 85% higher than h on the plain Si and SiNW surfaces, respectively. In addition, the S1300 surface did not experience a noticeable heat transfer degradation at high ΔT_{sub} .

The maximum heat transfer coefficient (h_{max}) on the 3D hybrid surfaces can be estimated as

$$h_{\text{max}} \sim h_{\text{DWC}}(1 - \varepsilon) + h_{\text{FWC}}\varepsilon \quad (1)$$

where h_{DWC} of $\sim 68 \pm 12$ $\text{kW}\cdot\text{m}^{-2}\cdot\text{K}^{-1}$ can be obtained from h on the SiNW surface at low $\Delta T_{\text{sub}} \sim 2$ K, and $h_{\text{FWC}} \sim 16 \pm 2$ $\text{kW}\cdot\text{m}^{-2}\cdot\text{K}^{-1}$ can be obtained from h on the plain Si surface at $\Delta T_{\text{sub}} \sim 2$ K. Using the prescribed ε of 40%, $h_{\text{max}} \sim 50 \pm 9$ $\text{kW}\cdot\text{m}^{-2}\cdot\text{K}^{-1}$ can be expected on the 3D hybrid surface. The discrepancy between the experimentally obtained h and h_{max} on the 3D hybrid surfaces occurred because parts of the hydrophobic regions on the 3D hybrid surfaces were covered by large liquid droplets or liquid bridges.

The q values on the studied surfaces shown in **Figure 4D** were obtained from Newton's cooling law $q = h \cdot \Delta T_{\text{sub}}$ with the measured h and the given ΔT_{sub} . Compared with q obtained on the SiNW surface, q was significantly enhanced on the 3D hybrid surfaces. The figure shows that the S1300 surface had the best condensation heat transfer among all of the surfaces. q on the S1300 hybrid surface was enhanced by 84% and by 225% from q on the SHB SiNW surface and from q on the plain Si

surface at $\Delta T_{\text{sub}} \sim 18$ K, respectively.

The maximum reported q on state-of-the-art micro/nanostructured SHB surfaces is $280 \text{ kW}\cdot\text{m}^{-2}$.²⁵ In this work, $q \sim 650 \text{ kW}\cdot\text{m}^{-2}$ was obtained on the S1300 surface, which pushes the current boundary of the condensation heat transfer. It is worth noting that the flooding heat flux was not reached on the S1300 surface even at the highest q of $650 \text{ kW}\cdot\text{m}^{-2}$ ($\Delta T_{\text{sub}} \sim 18$ K).

Concluding remarks

We demonstrated that 3D hybrid surfaces consisting of SHB SiNW arrays and hydrophilic microchannels can exhibit superior condensation heat transfer performance. In addition, the hydrophilic microchannels on 3D hybrid surfaces can confine the liquid film thickness, and liquid bridges formed on the surfaces can be self-removed. Both of these characteristics prevent the 3D hybrid surfaces from flooding at a high ΔT_{sub} . In addition, thin liquid film of $\sim 50 \text{ }\mu\text{m}$ in the microchannels can reduce the thermal resistance.

Moreover, liquid droplets formed at the SiNW regions on a 3D hybrid surface can be efficiently removed by the coalesce-induced jumping motion at low ΔT_{sub} . At medium and high ΔT_{sub} , the liquid droplets formed at the SiNW regions can be dragged into the microchannels, which reduces D_d at medium and high ΔT_{sub} . Furthermore, a large v was formed in the hydrophilic microchannels at high ΔT_{sub} . The small D_d and large v , the confined liquid film area, and the thin film thickness on the 3D hybrid surfaces enhanced h on the 3D hybrid surfaces at high ΔT_{sub} .

The h value of $37 \text{ kW}\cdot\text{m}^{-2}\cdot\text{K}^{-1}$ at $\Delta T_{\text{sub}} \sim 18$ K on the S1300 surface was 213% and 85% higher than h on the plain Si surface and the SHB SiNW surface, respectively. Even more remarkably, a record high heat flux of $650 \text{ kW}\cdot\text{m}^{-2}$ (at $\Delta T_{\text{sub}} \sim 18$ K) was obtained on the S1300 surface, which exceeded the highest reported heat flux ($q \sim 280 \text{ kW}\cdot\text{m}^{-2}$) in the literature. The results obtained in this work suggest that a 3D hybrid surface can be applied to enhance the heat transfer in various systems involving condensation.

ACKNOWLEDGMENTS

This work was supported by the Ministry of Science and Technology of Taiwan under grant MOST 105-2221-E-009-007-MY3.

AUTHOR CONTRIBUTIONS

C.-W. L. and M.-C. L. designed the research and experiments. Y.-C. C. and M.-H. Y. carried out the sample fabrication and characterization and conducted the condensation experiments. C.-W. L. and M.-C. L. wrote the manuscript. All authors

participated in the discussion of the research.

DECLARATION OF INTERESTS

The authors declare no competing interests.

EXPERIMENTAL PROCEDURES

Fabrication of 3D Hybrid Surfaces

The fabrication of the 3D hybrid surfaces included three parts: (1) microchannel fabrication, (2) SiNW synthesis, and (3) hydrophobic layer coating. A schematic of the fabrication procedure is shown in **Figure S1** in the Supplemental Information.

The fabrication process is as follows: (a) We coated a 10- μm -thick layer of AZ4620 photoresist (PR) using a PR spinner, and the PR was patterned on a Si wafer using the photolithography process; (b) we used deep reactive ion etching (DRIE) to etch the microchannels with a depth of 50 μm , and the residue PR was removed from the Si wafer; (c) to form the interlaced SiNW array regions, a thin layer of low-stress Si_3N_4 serving as an etching stopper layer with a thickness of ~ 450 nm was deposited by using the low-pressure chemical vapor deposition (LPCVD) method; (d) a thin layer of PR was spin-coated and patterned to protect the bottom and sidewall of the microchannels, and the exposed Si_3N_4 regions were anisotropically etched away by using DRIE; (e) 15- μm -height SiNW arrays were vertically etched on the bare Si regions, where the synthesis of the SiNW followed the same procedure as that reported in our previous works;³⁶ (g) the residual Si_3N_4 layer was subsequently removed by RIE; (h) a thin layer of PR was spin-coated and patterned in the microchannel regions; and (i) superhydrophobic SiNW arrays were obtained by fully coating the SiNW arrays with a thin layer (~ 60 nm) of polytetrafluoroethylene (Dupont, Teflon[®]) by using inductively coupled plasma RIE.

At the end, to bond the sample with the copper stage, the backside of the sample was consecutively sputtered with a thin chrome layer (~ 50 nm), a thin nickel layer (~ 50 nm), and a thin copper layer (~ 100 nm).

Condensation Heat Transfer Experimental System

The closed system for measuring the condensation heat transfer coefficients on the surfaces is shown in **Figure S2A** in the SI. The system had four major parts: a vapor generator, condensation chamber, test section, and impingement cooling system. The vapor generator was a cylindrical water tank with four cartridge heaters (~ 1 kW in total) embedded at the bottom of the tank to generate water vapor. Each heater was capable of supplying 1125 W.

The condensation chamber consisted of a cylindrical stainless steel T-tube with

the dimensions of 20 cm in diameter and 30 cm in height. A 15-cm-diameter sight window was equipped in the chamber wall to observe the condensation processes. Visualization of the condensation dynamics was achieved by a high-speed camera through the sight window. The condensation chamber was embedded with a pressure transmitter (Yokogawa, EJX510A) and five T-type thermocouples through the feedthroughs (Kurt J. Lesker, KF40) to monitor the pressure and temperature in the chamber, respectively. The test section consisted of a copper block and two Teflon® blocks.

The test section was mounted inside the condenser chamber. The Teflon blocks surrounding the copper block were for thermal insulation. The sample (2 cm in width, 4 cm long, and 500 μm thick) was vertically mounted on the copper stage by using Tin bonding at the interface to reduce the thermal contact resistance. A schematic of the test section is shown in **Figures S2B** and **S2C**. Two thermocouples (TCs) were bonded at the backside of the sample to measure the surface temperature, and two TCs were wired through the holes created at the side wall of the copper block to the center of the copper block to measure the temperature gradient. The obtained temperature gradient was employed to calculate the heat flux through the copper block.

An impingement cooling system was connected to the backside of the copper block. This can provide sufficient cooling capacity for dissipating the condensate heat (a maximum cooling capacity of 2 kW). The details of the impingement cooler can be found in our previous work.²¹ A constant water flow rate of 22 L/min was applied at the inlet of the impingement cooler, and the temperature of the water flow could be adjusted to control the degree of subcooling on the studied surfaces. The obtained data were transferred to a data acquisition system for data processing (Agilent, 34901A).

To conduct the condensation heat transfer experiments, a vacuum pump was used to maintain the condensation chamber and vapor generator at ~ 6 Pa for 1 h before the vapor generator was filled with degassed deionized (DI) water. To further reduce the noncondensable gas (NCG) effect, DI water was first degassed for 2 h.

After degassing, the saturated vapor flowed through a stainless steel tube to the condensation chamber, and a vapor distributor (a 1-cm-thick stainless disk with several 1-mm-diameter holes) was installed at the vapor inlet to spread the vapor flow uniformly throughout the condensation chamber. By adjusting the applied power of the cartridge heaters in the vapor generator, the pressure of the condensation chamber was controlled at 47 kPa with a corresponding saturation temperature of 80 °C. The concentration of the NCG in the experimental system was $\sim 0.5\%$.

Condensation Experiments using Environmental Scanning Electron Microscope

(ESEM)

The condensation sample in the ESEM had dimensions of 2 mm × 2 mm × 500 μm (width × length × height). The sample was attached to the surface of the copper stage at a 90° tilted angle using silver paste (SPI Supplies, USA). The copper stage was directly placed on the Peltier cooler. The condensation experiments were conducted under controlled conditions in which the wall temperature was maintained at 0 ± 0.2 °C and the pressure of the chamber was at 6 Torr (corresponding to the water saturation temperature of 3.91 °C). The absolute uncertainties for the chamber pressure and for the Peltier cooler temperature were estimated to be ± 0.1 Torr and ± 0.2 °C, respectively. The acceleration voltage, working distance, and emission current in the ESEM were maintained at 20 kV, ~10 mm, and ~10 μA, respectively.

Methodology for Determining Thin Film Velocity

The thin film velocity (v) in the microchannels was experimentally determined by tracking the blurry spots in the liquid film in the microchannels. The liquid droplets dragged into the microchannels resulted in convex menisci exhibiting as blurry spots (see **Figure S4**). v in the liquid film can be approximately obtained by dividing the displacements of the blurry spots by the corresponding time interval. In addition, v on the plain Si surface in the FWC was theoretically calculated by using Nusselt's theory. The details of the calculation can be found in the SI.

SUPPLEMENTAL INFORMATION

Three condensation videos and additional information on (1) the fabrication of the 3D hybrid surfaces, (2) contact angles on the studied surfaces, (3) condensation heat transfer experimental system and test section, (4) data reduction, (5) uncertainty analysis, (6) calculation of the heat transfer coefficient and the thin film velocity in the FWC, (7) heat loss simulation, and (8) method for determining the film velocity on the 3D hybrid surface can be found with this article online at XXXX.

REFERENCES

- (1) Cho, H.J., Preston, D.J., Zhu, Y. and Wang, E.N. (2017). Nanoengineered materials for liquid–vapour phase-change heat transfer. *Nat. Rev. Mater.* 2, 16092.
- (2) Attinger, D., Frankiewicz, C., Betz, A.R., Schutzius, T.M., Ganguly, R., Das, A., Kim, C.-J. and Megaridis, C.M. (2014). Surface engineering for phase change heat transfer: A review. *MRS Energy & Sustainability I*, 1-40.
- (3) Liu, B.-T., Chien, K.-H. and Wang, C.-C. (2004). Effect of working fluids on organic rankine cycle for waste heat recovery. *Energy* 29, 1207-1217.
- (4) Humplik, T., et al. (2011). Nanostructured materials for water desalination.

Nanotechnology 22, 292001.

- (5) Boreyko, J.B. and Chen, C.-H. (2013). Vapor chambers with jumping-drop liquid return from superhydrophobic condensers. *Int. J. Heat Mass Transfer* 61, 409-418.
- (6) Wen, R., Ma, X., Lee, Y.-C. and Yang, R. (2018). Liquid-vapor phase-change heat transfer on functionalized nanowired surfaces and beyond. *Joule* 2, 2307-2347.
- (7) Kim, H., Yang, S., Rao, S.R., Narayanan, S., Kapustin, E.A., Furukawa, H., Umans, A.S., Yaghi, O.M. and Wang, E.N. (2017). Water harvesting from air with metal-organic frameworks powered by natural sunlight. *Science* 356, 430-434.
- (8) Tu, Y., Wang, R., Zhang, Y. and Wang, J. (2018). Progress and expectation of atmospheric water harvesting. *Joule* 2, 1452-1475.
- (9) Hou, Y., Shang, Y., Yu, M., Feng, C., Yu, H. and Yao, S. (2018). Tunable water harvesting surfaces consisting of biphilic nanoscale topography. *ACS Nano* 12, 11022-11030.
- (10) Li, X., Min, X., Li, J., Xu, N., Zhu, P., Zhu, B., Zhu, S. and Zhu, J. (2018). Storage and recycling of interfacial solar steam enthalpy. *Joule* 2, 2477-2484.
- (11) Miljkovic, N., Preston, D.J., Enright, R. and Wang, E.N. (2014). Jumping-droplet electrostatic energy harvesting. *Appl. Phys. Lett.* 105, 013111.
- (12) Preston, D.J., Mafra, D.L., Miljkovic, N., Kong, J. and Wang, E.N. (2015). Scalable graphene coatings for enhanced condensation heat transfer. *Nano Letters* 15, 2902-2909.
- (13) Hou, Y., Yu, M., Chen, X., Wang, Z. and Yao, S. (2014). Recurrent filmwise and dropwise condensation on a beetle mimetic surface. *ACS Nano* 9, 71-81.
- (14) Oh, J., Zhang, R., Shetty, P.P., Krogstad, J.A., Braun, P.V. and Miljkovic, N. (2018). Thin film condensation on nanostructured surfaces. *Adv. Funct. Mater.* 28, 1707000.
- (15) Park, K.-C., Kim, P., Grinthal, A., He, N., Fox, D., Weaver, J.C. and Aizenberg, J. (2016). Condensation on slippery asymmetric bumps. *Nature* 531, 78-82.
- (16) Preston, D.J., Wilke, K.L., Lu, Z., Cruz, S.S., Zhao, Y., Becerra, L.L. and Wang, E.N. (2018). Gravitationally driven wicking for enhanced condensation heat transfer. *Langmuir* 34, 4658-4664.
- (17) Chen, X., Wu, J., Ma, R., Hua, M., Koratkar, N., Yao, S. and Wang, Z. (2011). Nanograssed micropyrarnidal architectures for continuous dropwise condensation. *Adv. Funct. Mater.* 21, 4617-4623.
- (18) Rose, J. (2002). Dropwise condensation theory and experiment: A review. *Proc. Inst. Mech. Eng. A* 216, 115-128.
- (19) Chen, C.-H., Cai, Q., Tsai, C., Chen, C.-L., Xiong, G., Yu, Y. and Ren, Z. (2007). Dropwise condensation on superhydrophobic surfaces with two-tier roughness. *Appl. Phys. Lett.* 90, 173108.

- (20) Yan, X., et al. (2019). Droplet jumping: Effects of droplet size, surface structure, pinning, and liquid properties. *ACS Nano* 1309-1323.
- (21) Lu, M.-C., Lin, C.-C., Lo, C.-W., Huang, C.-W. and Wang, C.-C. (2017). Superhydrophobic Si nanowires for enhanced condensation heat transfer. *Int. J. Heat Mass Transfer* 111, 614-623.
- (22) Miljkovic, N., Enright, R. and Wang, E.N. (2012). Effect of droplet morphology on growth dynamics and heat transfer during condensation on superhydrophobic nanostructured surfaces. *ACS Nano* 6, 1776-1785.
- (23) Lo, C.-W., Wang, C.-C. and Lu, M.-C. (2014). Scale effect on dropwise condensation on superhydrophobic surfaces. *ACS Appl. Mater. Interfaces* 6, 14353-14359.
- (24) Feng, J., Pang, Y., Qin, Z., Ma, R. and Yao, S. (2012). Why condensate drops can spontaneously move away on some superhydrophobic surfaces but not on others. *ACS Appl. Mater. Interfaces* 4, 6618-6625.
- (25) Wen, R., Xu, S., Ma, X., Lee, Y.-C. and Yang, R. (2018). Three-dimensional superhydrophobic nanowire networks for enhancing condensation heat transfer. *Joule* 2, 269-279.
- (26) Cheng, J., Vandadi, A. and Chen, C.-L. (2012). Condensation heat transfer on two-tier superhydrophobic surfaces. *Appl. Phys. Lett.* 101, 131909.
- (27) Miljkovic, N., Enright, R., Nam, Y., Lopez, K., Dou, N., Sack, J. and Wang, E.N. (2012). Jumping-droplet-enhanced condensation on scalable superhydrophobic nanostructured surfaces. *Nano Letters* 13, 179-187.
- (28) Ölçeroğlu, E. and McCarthy, M. (2016). Self-organization of microscale condensate for delayed flooding of nanostructured superhydrophobic surfaces. *ACS Appl. Mater. Interfaces* 8, 5729-5736.
- (29) Alwazzan, M., Egab, K., Peng, B., Khan, J. and Li, C. (2017). Condensation on hybrid-patterned copper tubes (i): Characterization of condensation heat transfer. *Int. J. Heat Mass Transfer* 112, 991-1004.
- (30) Yao, C., Garvin, T., Alvarado, J., Jacobi, A., Jones, B. and Marsh, C. (2012). Droplet contact angle behavior on a hybrid surface with hydrophobic and hydrophilic properties. *Appl. Phys. Lett.* 101, 111605.
- (31) Preston, D.J. and Wang, E.N. (2018). Jumping droplets push the boundaries of condensation heat transfer. *Joule* 2, 205-207.
- (32) Enright, R., Miljkovic, N., Alvarado, J.L., Kim, K. and Rose, J.W. (2014). Dropwise condensation on micro- and nanostructured surfaces. *Nanoscale Microscale Thermophys. Eng.* 18, 223-250.
- (33) Togonal, A., He, L. and Roca i Cabarrocas, P. (2014). Effect of wettability on the agglomeration of silicon nanowire arrays fabricated by metal-assisted chemical

etching. *Langmuir* 30, 10290-10298.

(34) Lo, C.W., Wang, C.C. and Lu, M.C. (2014). Spatial control of heterogeneous nucleation on the superhydrophobic nanowire array. *Adv. Funct. Mater.* 24, 1211-1217.

(35) Boreyko, J.B. and Chen, C.-H. (2009). Self-propelled dropwise condensate on superhydrophobic surfaces. *Phys. Rev. Lett.* 103, 184501.

(36) Chen, R., Lu, M.-C., Srinivasan, V., Wang, Z., Cho, H.H. and Majumdar, A. (2009). Nanowires for enhanced boiling heat transfer. *Nano letters* 9, 548-553.

FIGURES

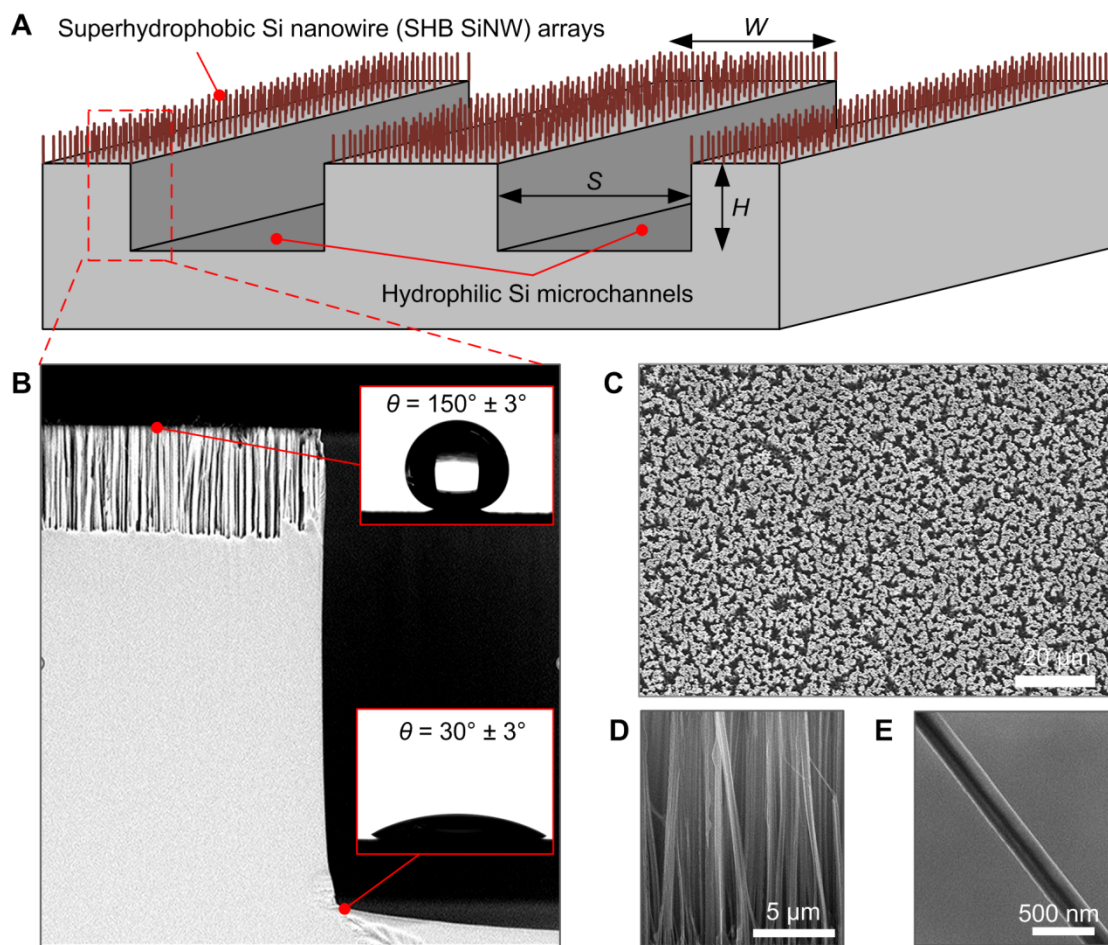


Figure 1. Surface Morphology and Structure Characterizations of Three-Dimensional (3D) Hybrid Surface. (A) Overview of 3D hybrid surface (not to scale). (B) Cross-sectional SEM image of microchannel and SiNW array. Insets show corresponding CAs. (C) Top-view SEM image of SiNW array, showing dense nanowire distribution. (D) Enlarged side-view SEM image of vertically aligned Si nanowires. (E) SEM image of single Si nanowire whose diameter is in range of 50–300 nm.

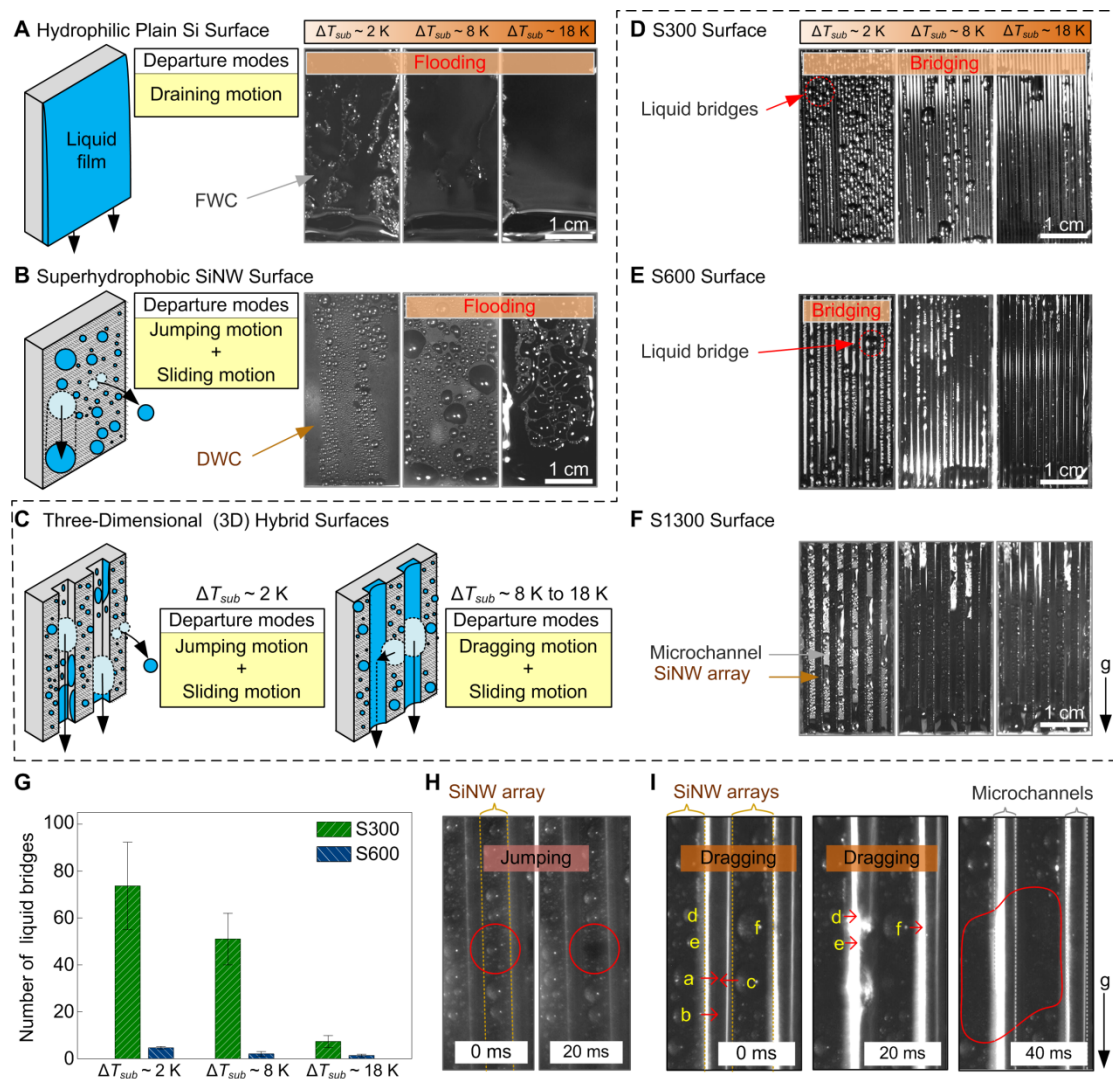


Figure 2. Departure Dynamics of Condensate on Studied Surfaces. (A) FWC on hydrophilic plain Si surface, (B) DWC on SHB SiNW surface, and (C) schematic diagrams of droplet departure modes on 3D hybrid surfaces. (D–F) Condensation dynamics of S300, S600, and S1300 surfaces at different ΔT_{sub} , respectively. (G) Number of liquid bridges at different subcooling temperatures on 3D hybrid surfaces. (H) Jumping motion was observed in SiNW array regions on S300 surface. (I) Liquid droplets formed on SiNW array regions were dragged into microchannels on S600 surface.

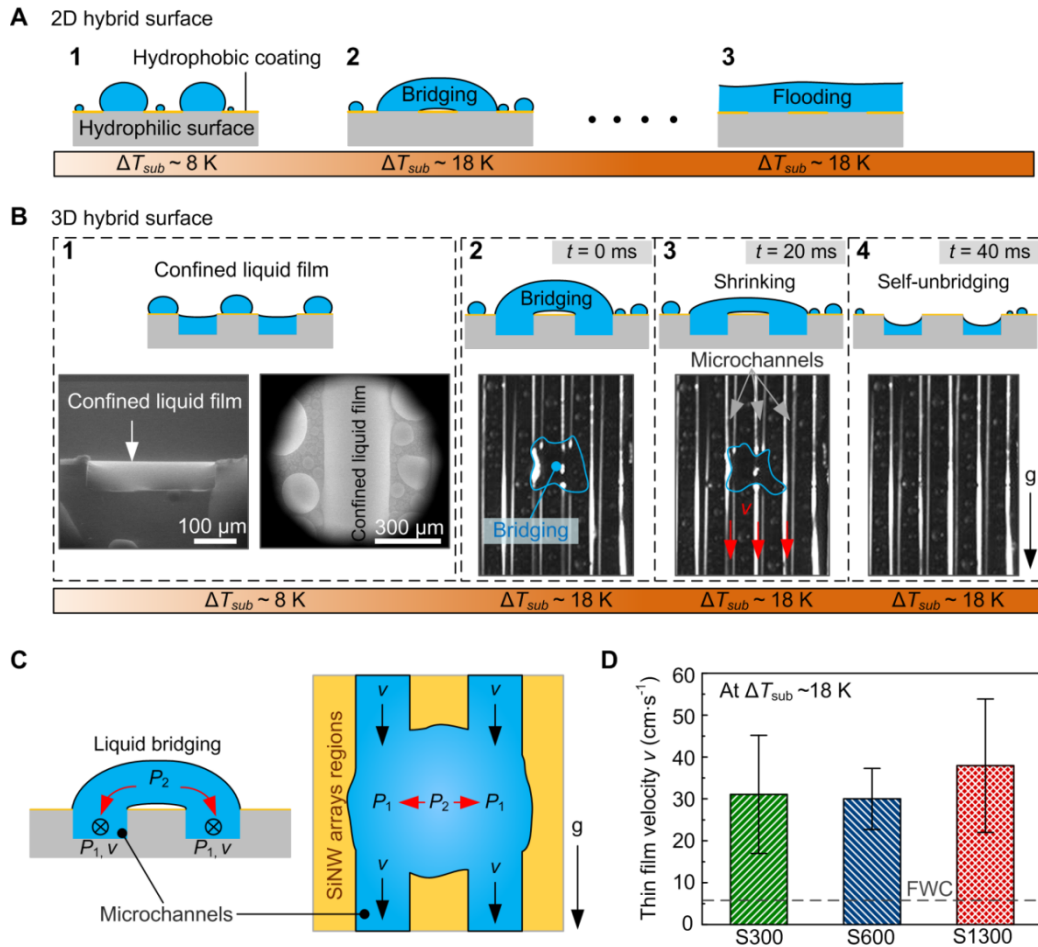


Figure 3. Confined Liquid Film and Self-unbridging Phenomenon on 3D Hybrid Surfaces. (A) Liquid bridge-induced flooding on traditional 2D hybrid surface. (B-1) Confined liquid film thickness in microchannel on S300 surface; DWC occurred concurrently in SiNW array regions on S300 surface. (B-2) Liquid bridge formed on S600 surface. (B-3) Liquid bridge absorbed into surrounding microchannels. (B-4) Liquid bridge disappeared 40 ms after formation. (C) Mechanism of self-unbridging phenomenon on 3D hybrid surfaces. (D) Measured liquid film velocity (v) in microchannels on 3D hybrid surfaces at $\Delta T_{sub} \sim 18 \text{ K}$; dashed line indicates theoretical film velocity in FWC.

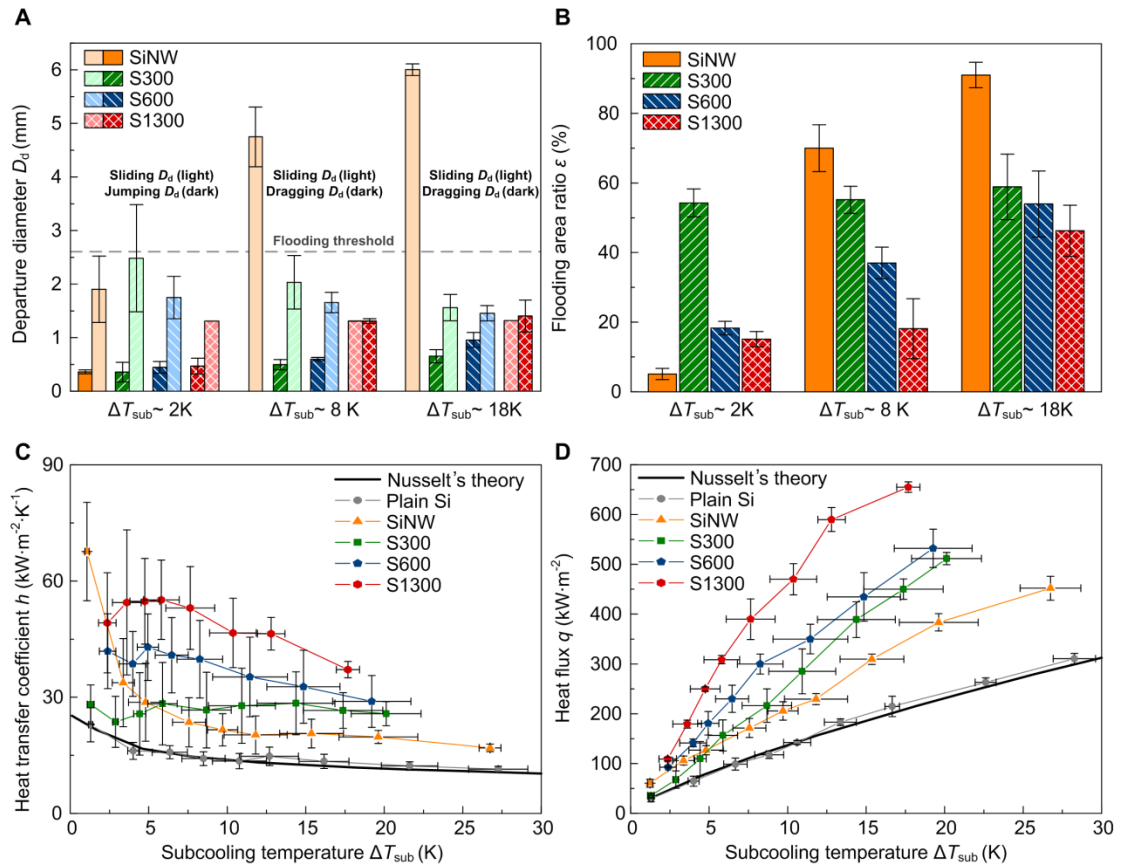
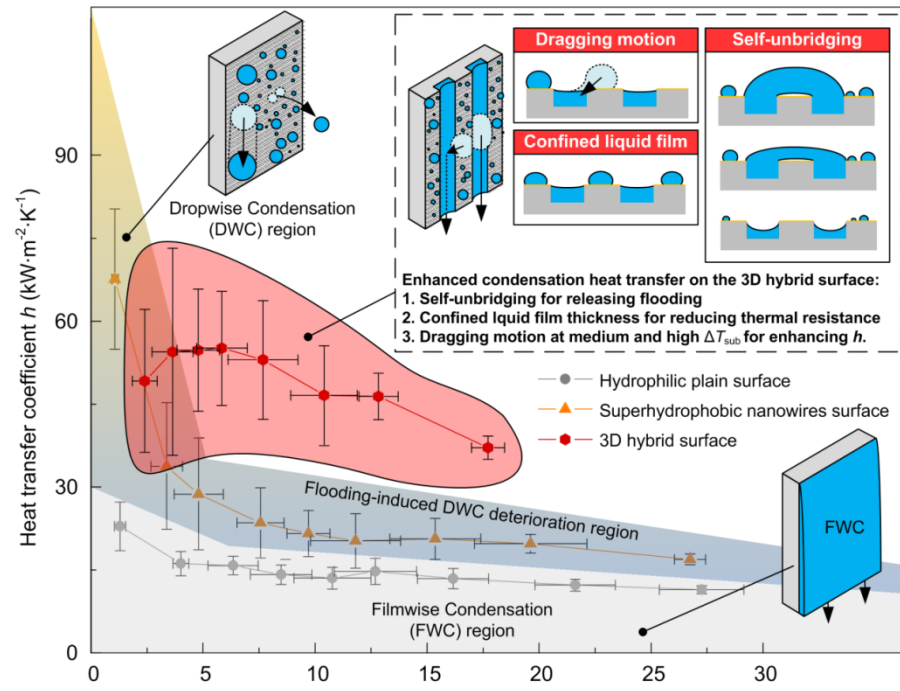


Figure 4. Quantitative Analysis of Condensation Phenomena and Condensation Heat Transfer on Studied Surfaces. (A) Departure diameters D_d on surfaces at three different ΔT_{sub} . (B) Flooding area ratio ϵ on surfaces at three different ΔT_{sub} . (C) Condensation heat transfer coefficient h as function of ΔT_{sub} on studied surfaces. (D) Condensation heat flux q as function of ΔT_{sub} on studied surfaces. Black solid lines in (C) and (D) represent theoretical calculations of h and q , respectively, from Nusselt theory. Error bars indicate standard deviations from three repeated experiments.

TABLE OF CONTENTS



JOULE

Supplemental Information

**Enhancing Condensation Heat Transfer on Three-
Dimensional Hybrid Surfaces**

*Ching-Wen Lo, Yu-Cheng Chu, Ming-Han Yan, and Ming-Chang Lu**

Fabrication of 3D Hybrid Surfaces

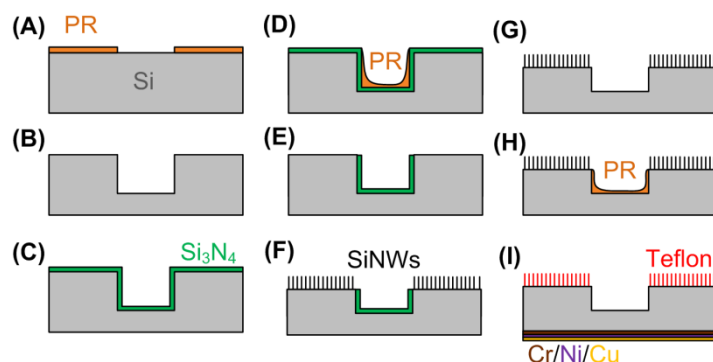


Figure S1. Fabrication procedure of three-dimensional hybrid surface. (A) patterning photoresist (PR) on the Si substrate; (B) deep reactive-ion etching of the microchannels; (C) depositing Si_3N_4 thin layer; (D) patterning PR on the Si_3N_4 layer; (E) etching away the Si_3N_4 layer and removing the PR; (F) synthesizing the Si nanowire array; (G) removing the residue Si_3N_4 ; (H) patterning PR; (I) Teflon coating on the SiNW array and Cr/Ni/Cu coating at the back side of sample. The film thicknesses of Cr, Ni and Cu were 50, 50, and 100 nm, respectively.

Contact Angles on Studied Surfaces

Table S1. Water Contact Angles on Studied Surfaces.

Name	θ [°]	θ_{adv} [°]	θ_{rec} [°]	θ_{CAH} [°]
Plan Si	$30^\circ \pm 3^\circ$	$88.5^\circ \pm 5^\circ$	$15.4^\circ \pm 4^\circ$	$\sim 73^\circ$
SiNW	$144.1^\circ \pm 1^\circ$	$152.5^\circ \pm 2^\circ$	$141.6^\circ \pm 4^\circ$	$\sim 11^\circ$
S1300	$74.8^\circ \pm 5^\circ$	$88.7^\circ \pm 1^\circ$	$11.7^\circ \pm 5^\circ$	$\sim 77^\circ$
S600	$106.5^\circ \pm 2^\circ$	$91.9^\circ \pm 5^\circ$	$17.6^\circ \pm 4^\circ$	$\sim 74^\circ$
S300	$109.1^\circ \pm 7^\circ$	$124.3^\circ \pm 8^\circ$	$31.6^\circ \pm 3^\circ$	$\sim 93^\circ$

θ , θ_{adv} , θ_{rec} , and θ_{CAH} are the equilibrium CA, advancing CA, receding CA, and contact angle hysteresis (CAH), respectively. The CAs on the 3D hybrid surfaces were measured in the direction along the microchannels. The values of the CAs were determined using Krüss drop shape analysis with an accuracy of 0.1°. The tested fluid was the deionized water and the CAs were obtained at the room temperature under the laboratory conditions. The equilibrium CAs on the solid surfaces were measured by gently depositing a liquid droplet of 10 μL volume on the surfaces through a microsyringe pump at the same injection rate of $\sim 190 \mu\text{L}\cdot\text{min}^{-1}$.

Condensation Heat Transfer Experimental System

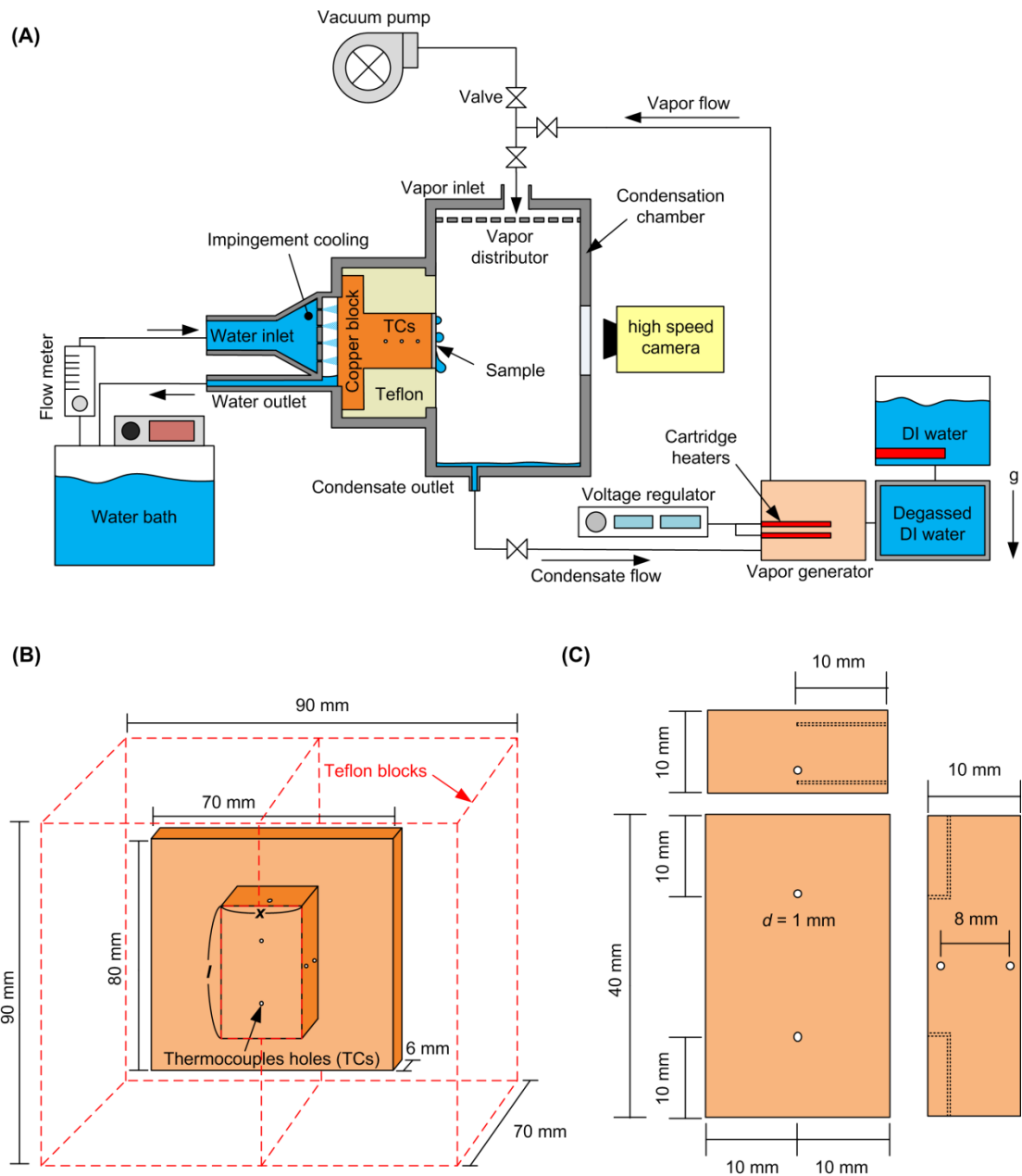


Figure S2. Schematic diagrams of condensation heat transfer experimental system and test section. (A) The experimental system consisting of four major parts: a vapor generator, a condenser, a test section, and an impingement cooling system. (B) The schematic of the test section. (C) The exploded view of the copper block.

Data Reduction

The heat transfer coefficient h was obtained from Newton's cooling law: $h = Q \cdot (A_c \cdot \Delta T_{\text{sub}})^{-1}$, where Q is heat transfer rate and A_c is the area of condensing surface (*i.e.*, 8 cm²). ΔT_{sub} is $T_v - T_w$, where T_v is the surrounding vapor temperature and T_w is the wall temperature on the condensing surface. The T_w was controlled by adjusting the temperature of the chilled water tank with a temperature fluctuation < 0.1 K. T_v was directly measured in the condensation chamber. In order to reduce thermal contact resistance, two thermocouples (TCs) were directly bonded at the backside of the condensing surface to obtain the average backside wall temperature (T_{bw}). Meanwhile, two TCs were welded at the center of the copper block through the holes on the side wall of the copper block (see **Figure S2B**). Using the two temperatures measured at the center of the copper block, the temperature gradient could be obtained. The temperature gradient was used to obtain the Q passing through the condensing surface. By assuming one-dimensional heat transfer, T_w can be obtained from $T_w = T_{\text{bw}} + Q \cdot L \cdot k_s^{-1} \cdot x^{-1} \cdot l^{-1}$, where L , x , l , and k_s are the thickness of Si wafer, sample width, sample length, and the thermal conductivity of silicon wafer, respectively. Si wafer thickness and its thermal conductivity were taken as 500 μm and 140 $\text{W} \cdot \text{m}^{-1} \cdot \text{K}^{-1}$, respectively.

Uncertainty Analysis

The experimental errors were analyzed using the error propagation theory. The obtained h in this work can be expressed as:

$$h = \frac{Q}{A_c \cdot \Delta T_{sub}} \quad (S1)$$

Using the error propagation theory, the uncertainties for the heat transfer rate (W_Q), for the condensing surface (W_{A_c}), and for the surface subcooling ($W_{\Delta T_{sub}}$) could be obtained from:

$$W_Q = \sqrt{\left[\frac{dh}{dk_c} W_{k_c} \right]^2 + 2 \left[\frac{dh}{dT} W_T \right]^2} \quad (S2)$$

$$W_{\Delta T_{sub}} = \sqrt{\left[\frac{d\Delta T_{sub}}{dT} W_T \right]^2 + \left[\frac{d\Delta T_{sub}}{dk_s} W_{k_s} \right]^2 + \left[\frac{d\Delta T_{sub}}{dl} W_l \right]^2 + \left[\frac{d\Delta T_{sub}}{dx} W_x \right]^2 + \left[\frac{d\Delta T_{sub}}{dL} W_L \right]^2 + \left[\frac{d\Delta T_{sub}}{dQ} Q \right]^2} \quad (S3)$$

$$W_{A_c} = \sqrt{\left[\frac{dA_c}{dx} W_x \right]^2 + \left[\frac{dA_c}{dl} W_l \right]^2} \quad (S4)$$

where W_{k_c} is the uncertainty of copper thermal conductivity and its value was taken as $15 \text{ W}\cdot\text{m}^{-1}\cdot\text{K}^{-1}$. W_x and W_l are the uncertainties of sample width and sample length, respectively, and their values were taken as 0.5 mm. W_T is the corresponding uncertainty of temperature and its value was taken as $0.2 \text{ }^\circ\text{C}$ according to the specification of the thermocouples. The uncertainty of the silicon sample thickness (W_L) was taken as $50 \text{ }\mu\text{m}$. The uncertainty of heat transfer coefficient (W_h) was obtained from:

$$W_h = \sqrt{\left[\frac{dh}{dQ} W_Q\right]^2 + \left[\frac{dh}{d\Delta T_{sub}} W_{\Delta T_{sub}}\right]^2 + \left[\frac{dh}{dA_c} W_{A_c}\right]^2} \quad (S5)$$

The calculated relative uncertainty of heat transfer coefficient h on the hydrophilic plain Si surface was from 48% at low ΔT_{sub} to 9% at high ΔT_{sub} . The large uncertainty at low subcooling was a result of a small temperature gradient in determining condensation heat transfer rate at a low ΔT_{sub} . The relative uncertainty of heat transfer coefficients on the superhydrophobic SiNW surface was from 45% at low ΔT_{sub} to 9% at high ΔT_{sub} . The relative uncertainties of heat transfer coefficients on S1300, S600 and S300 surfaces from low ΔT_{sub} to high ΔT_{sub} ranged from 14.6%–8%, 16.3%–8%, and 39.8%–8%, respectively.

The Heat Transfer Coefficient and Thin Film Velocity in FWC

The Nusselt theory was applied for the theoretical prediction of the FWC heat transfer coefficient:

$$h_{FWC} = \left[\frac{4 \cdot k_l \cdot \mu_l \cdot \Delta T_{sub} \cdot l}{g \cdot \rho_l \cdot (\rho_l - \rho_v) \cdot h_{lv}} \right]^{0.25} \quad (S6)$$

where k_l , μ_l , x , g , ρ_l , and ρ_v are the thermal conductivity of water ($k_l = 0.669 \text{ W} \cdot \text{m}^{-1} \cdot \text{K}^{-1}$), dynamics viscosity of water ($\mu_l = 35 \times 10^{-6} \text{ N} \cdot \text{s} \cdot \text{m}^{-2}$), characteristic condensation length ($l = 4 \text{ cm}$), gravitational acceleration ($g = 9.81 \text{ m} \cdot \text{s}^{-2}$), water density ($\rho_l = 971 \text{ kg} \cdot \text{m}^{-3}$), and vapor density ($\rho_v = 0.956 \text{ kg} \cdot \text{m}^{-3}$), respectively. In the equation, ΔT_{sub} was a controlled parameter.

The v can be obtained by the volume conservation: $v = V \cdot A^{-1}$, where A is the cross-sectional area of liquid film which is equal to the product of liquid film thickness δ and sample width ($x = 2 \text{ cm}$) and the V is overall condensed volume flow rate. The thickness of liquid film δ was obtained from: $\delta \sim k_l \cdot h_{FWC}^{-1}$. Meanwhile, the V was calculated from $V = Q \cdot \rho_l^{-1} \cdot h_{lv}^{-1}$ where Q is total heat transfer rate which was obtained from the Newton's cooling law: $Q = h_{FWC} \cdot (l \cdot x) \cdot \Delta T_{sub}$ in which the sample length (l) and the sample width (x) were 4 and 2 cm, respectively. By substituting the obtained Q and δ into the volume conservation equation, $v = x \cdot h_{FWC}^2 \cdot \Delta T_{sub} \cdot \rho_l^{-1} \cdot h_{lv}^{-1} \cdot k_l^{-1}$ can be obtained. Using the $\Delta T_{sub} = 18 \text{ K}$, we obtained $v = 6 \text{ cm/s}$.

Heat Loss Simulation

We used ANSYS-Fluent to estimate the heat loss of the condensation system. **Figure S3A** shows the simplified model of the test section. Water channel connected at the backside of the copper block ($2 \times 4 \times 2 \text{ cm}^3$) was used to mimic the impingement cooling system. The copper block was surrounded by Teflon for thermal insulation to reduce the heat loss. The heat transfer coefficients obtained from the experiments were applied on the top heat transfer surface and the rest of the exposed areas were applied to the nature convection condition. The applied heat transfer coefficients on various condensation heat transfer surfaces and the heat transfer coefficient for nature convection were listed in **Table S2**. A constant water flow rate with a given inlet temperature was assigned at the inlet of the square channel and the boundary condition for the outlet of the channel was set at one atmosphere. The boundary conditions and material properties are also shown in **Table S2**. **Figure S3B** and **3C** give the side-view and the top-view of temperature distribution from the simulation result on the S1300 surface. Using the temperature gradient in the copper block obtained from the simulation result, a conduction heat transfer rate through the copper block could be obtained by the Fourier's law. At the same time, the condensation heat transfer rates through the condensation surfaces could also be obtained from the simulation. As a result, the heat loss of the system could be determined. The percentages of heat losses on the hydrophilic plain Si surface, superhydrophobic SiNW surface, S1300, S600, S300 surfaces were 12.8%, 6.9%, 8%, 8.7%, and 10.9% respectively.

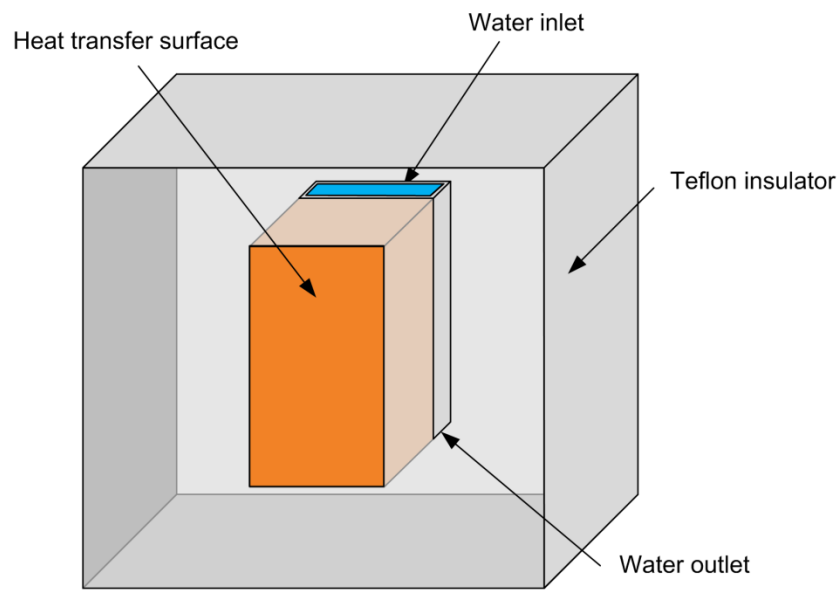
Table S2 Simulation Boundary Conditions and Materials' Properties.

h on plain Si surface ($\text{kW}\cdot\text{m}^{-2}\cdot\text{K}^{-1}$)	22.8
h on SiNW surface ($\text{kW}\cdot\text{m}^{-2}\cdot\text{K}^{-1}$)	67.6
h on S1300 surface ($\text{kW}\cdot\text{m}^{-2}\cdot\text{K}^{-1}$)	49.1

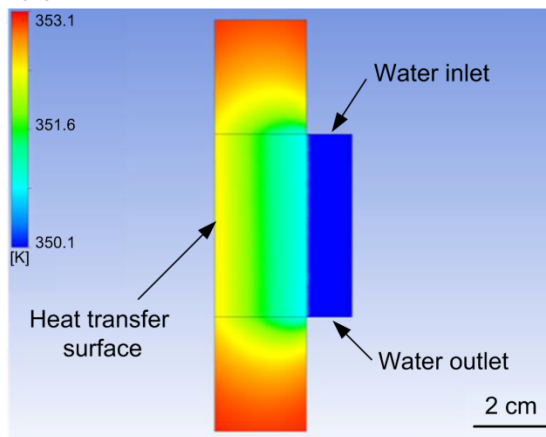
h on S600 surface ($\text{kW}\cdot\text{m}^{-2}\cdot\text{K}^{-1}$)	41.8
h on S300 surface ($\text{kW}\cdot\text{m}^{-2}\cdot\text{K}^{-1}$)	28.1
Natural convection heat transfer coefficient ($\text{kW}\cdot\text{m}^{-2}\cdot\text{K}^{-1}$)	0.015
Water flow rate at the channel ($\text{m}\cdot\text{s}^{-1}$)	10
Water inlet temperature ($^{\circ}\text{C}$)	77
Environmental temperature ($^{\circ}\text{C}$)	80
Copper thermal conductivity ($\text{W}\cdot\text{m}^{-1}\cdot\text{K}^{-1}$)	392
Teflon thermal conductivity ($\text{W}\cdot\text{m}^{-1}\cdot\text{K}^{-1}$)	0.15

h is the heat transfer coefficient.

(A)



(B)



(C)

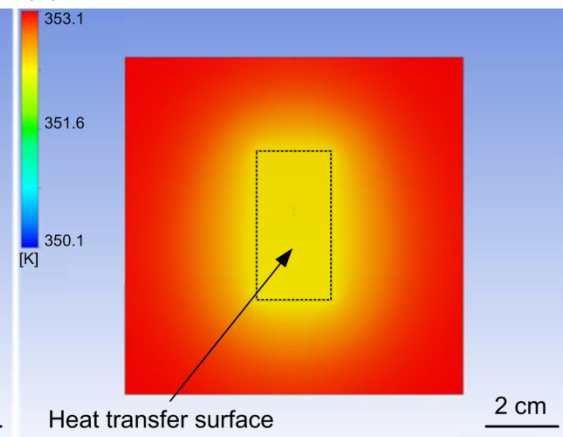


Figure S3. Heat Loss Simulation for Condensation Experiments. (A) Schematic of a simplified test section for simulation, (B) top-view temperature distribution, and (c) the cross-sectional view temperature distribution, where the unit of temperature is in Kelvin.

Methodology for Determining Thin Film Velocity

Thin film velocity (v) in microchannels was experimentally determined by tracking the blurry spots in the liquid film in the microchannels. The liquid droplets dragged into the microchannels resulted in convex menisci exhibiting as the blurry spots (see **Figure S4**). The v in the liquid film can be approximately obtained by dividing the displacements of the blurry spots by the corresponding time interval.

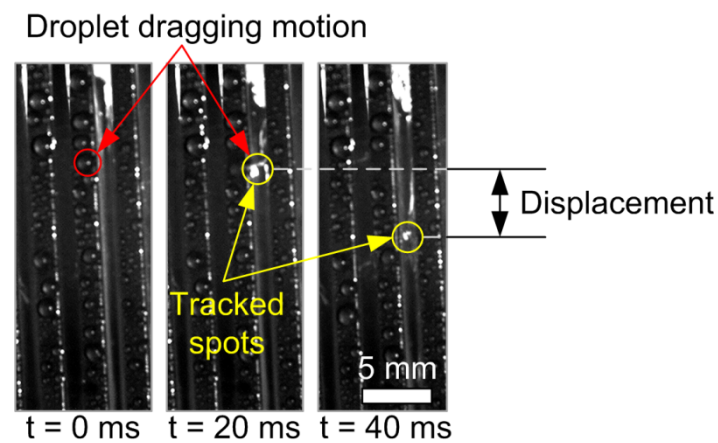


Figure S4. Experimental Methodology for Determining the Thin Film Velocity.

The time-sequences condensation images showing the blurry spots used in determining the film velocity in the microchannels on the S1300 surface at $\Delta T_{\text{sub}} \sim 18$ K, where gravity is downward.